J Mater Sci: Mater Electron **(2023) 34:2236**

Phase transformation and heterojunction nanostructures of bismuth iron oxide

Chunxin Xu[1], Yufei Wang[1,*], Qin Wang[1], Jian Li[1], and Long Yan[1,*]

[1] *Shaanxi Key Laboratory of Low Metamorphic Coal Clean Utilization, School of Chemistry and Chemical Engineering, Yulin University, Yulin 719000, People's Republic of China*

Received: 19 August 2023
Accepted: 1 November 2023
Published online: 3 December 2023

ABSTRACT

The construction of an efficient bismuth iron oxide shows great potential in excellent crystal structure properties and visible light photocatalysis. However, it is challenging to synthesize nanostructures with the desired morphologies. For the first time, the bismuth iron oxide is fabricated using sol–gel synthesis method, exhibiting the desired crystallite size and tuning the types of heterojunction nanostructures by regulating the concentration of Fe^{3+} and calcination temperature. As a result, the feeding ratios of bismuth ferrite materials $Bi_2Fe_4O_9$, $BiFeO_3/Bi_2Fe_4O_9$, $BiFeO_3$, $BiFeO_3/Bi_{25}FeO_{40}$, and $Bi_{25}FeO_{40}$ are 2:1, 1.5:1, 1:1, 0.75:1, 0.5:1, and 0.04:1, respectively. Besides, the calcination temperature not only influences the granularity of bismuth iron oxide but also promotes the phase transformation from $BiFeO_3$ to $Bi_2Fe_4O_9$. Moreover, $BiFeO_3/Bi_2Fe_4O_9$ and $BiFeO_3/Bi_{25}FeO_{40}$ heterojunction nanostructures display strong interactions between $BiFeO_3$–$Bi_2Fe_4O_9$ and $Bi_{25}FeO_{40}$. Besides, $BiFeO_3/Bi_{25}FeO_{40}$ heterojunction nanostructures exhibit obvious grain boundary with the smallest bandgap. This study presents far-reaching implications and provides pathways to prepare $BiFeO_3/Bi_2Fe_4O_9$ and $BiFeO_3/Bi_{25}FeO_{40}$ heterojunction nanostructures.

1 Introduction

Bismuth iron oxide, as a typical semiconductor, is widely employed because of its narrow bandgap and excellent storage, sensing, and multiferroic properties [1, 2]. However, further performance optimization of bismuth ferrite is a difficult task because the preparation of heterojunction nanostructures requires complex reaction conditions [3, 4]. Hence, further improving the catalytic performance of bismuth ferrite for photocatalytic reactions by doping other metallic atoms and modifying the morphology of what requires the pursuit of heterojunction nanostructures with a controllable crystal phase [5–7]. Moreover, the functions of redox activity, photocatalytic performance, and electron donor–acceptor pair in heterojunction materials are diverse and powerful [8, 9]. Among these several strategies, constructing heterojunction structures can significantly improve the utilization of

Chunxin Xu and Yufei Wang have contributed equally to this work.

Address correspondence to E-mail: wangyufei0003@163.com; ylyanlong@126.com

https://doi.org/10.1007/s10854-023-11576-3

electron holes, while enhancing the electronic mobility and showing excellent optoelectronic properties [10–12].

Numerous research efforts have been devoted to fabricate the name material with a desirable structure and excellent ferroelectric properties. However, the influence of crystal structure on morphology, crystallite size, and performance of bismuth iron oxide is still limited. Furthermore, the structure–property relationship of bismuth iron oxide with a heterojunction nanostructure is relatively complex, whereas main reasons for the precise regulation of phase composition content and grain size of the heterojunction are still unknown. Hence, the phase composition of optimal design and precision synthesis of $BiFeO_3/Bi_2Fe_4O_9$ and $BiFeO_3/Bi_{25}FeO_{40}$ heterojunction nanostructures through the feed ratio of Bi, Fe, and calcination temperature by simple Fe^{3+} doping. These findings present far-reaching implications and provide pathways for the further development of heterojunction nanostructure with metallic doping of bismuth iron oxide.

Based on the aforementioned discussion, we designed and prepared $BiFeO_3/Bi_2Fe_4O_9$ and $BiFeO_3/Bi_{25}FeO_{40}$ heterojunction nanostructures by the sol–gel method. Herein, the preparation of heterojunction nanostructures is achieved by adjusting the crystallite size and phase composition of bismuth iron oxide. Furthermore, $BiFeO_3/Bi_2Fe_4O_9$ and $BiFeO_3/Bi_{25}FeO_{40}$ heterojunction nanostructures display strong interactions between $BiFeO_3$-$Bi_2Fe_4O_9$ and $Bi_{25}FeO_{40}$. Moreover, $BiFeO_3/Bi_{25}FeO_{40}$ heterojunction nanostructures exhibit obvious grain boundaries with a small bandgap. This study presents a simple route to prepare $BiFeO_3/Bi_2Fe_4O_9$ and $BiFeO_3/Bi_{25}FeO_{40}$ dual heterojunction nanostructures.

2 Experimental section

Bismuth iron oxide powder was prepared by the citric acid-based sol–gel method. Different molar ratios of $Bi(NO_3)_3{\cdot}5H_2O$ (Tianjin Kermel Chemical Reagent Co. Ltd., China) and $Fe(NO_3)_3{\cdot}9H_2O$ (Tianjin Tianli Chemical Reagents Co. Ltd., China) were mixed in a beaker under constant stirring to obtain a mixture. Then, 20 mL of ethylene glycol methyl ether (Tianjin Kermel Chemical Reagent Co. Ltd., China) and 20 µL of 0.2-M HNO_3 (Tianjin Kermel Chemical Reagent Co. Ltd., China) were added into a three-necked flask and magnetically stirred in a KQ-300 VDE ultrasonic cleaner (Kunming Ultrasonic Instruments Co. Ltd., China) to obtain a clear solution. Then, 0.08 mol of citric acid (Tianjin Zhiyuan Chemical Reagent Co. Ltd., China) and 10 mL of ethylene glycol (Tianjin Kermel Co. Ltd., China) were added under magnetic stirring. Secondly, the reaction vessel was placed in a DF-10IB water bath (Changzhou Nuoji Instruments Co. Ltd., China) at 60 °C for 1 h. The as-obtained dark/brown gel was dried in a drying oven at 60 °C and the dried sample was placed in a muffle furnace after grounding into powder in an agate crucible. Finally, the sample in the muffle furnace was treated at 200 °C for 30 min and, then, heated to a certain temperature for 60 min, followed by cooling to room temperature. The heating and cooling rates were kept at 4.7 °C min^{-1}. The as-prepared sample was taken out and characterized as bismuth ferrite powder.

The crystal structure of bismuth iron oxide was studied by an X-ray diffractometer (Bruker D8 Advance), equipped with a Cu Kα radiation source (λ = 1.5418 Å). The optical performance was measured using UV–vis spectroscopy (UV-2600) and X-ray photoemission spectroscopy (XPS) was performed using a Thermo SCIENTIFIC ESCALAB 250Xi spectrometer. The morphology and microstructure of the as-prepared materials were characterized by a scanning electron microscope (SEM, JSM-7800F) and transmission electron microscopy (TEM, JEOL-JEM 2100 F), equipped with a field emission gun operating at 200 kV.

3 Results and discussion

The structural characteristics of bismuth iron oxide were investigated comprehensively. As shown in Fig. 1a, at the calcination temperature of 550 °C, the diffraction peaks of bismuth ferrite oxide (BFO) at 22.49°, 31.80°, and 32.13° can be attributed to (101), (012), and (110) planes of $BiFeO_3$, respectively. When the calcination temperature is less than 550 °C, the peak at 2θ = 27.77° reveals the presence of Bi_2O_3, indicating that the low temperature is favorable for the precipitation of the impurity phase. When the annealing temperature is greater than 550 °C, the peak at 2θ = 29.72° corresponds to the $Bi_2Fe_4O_9$ phase. Hence, it can be inferred $BiFeO_3$ is quite unstable and easily transformed into Bi_2O_3 and $Bi_2Fe_4O_9$ due to its unstable structure [13]. Therefore, the high temperature is favorable for the precipitation of $Bi_2Fe_4O_9$ (JCPDS:

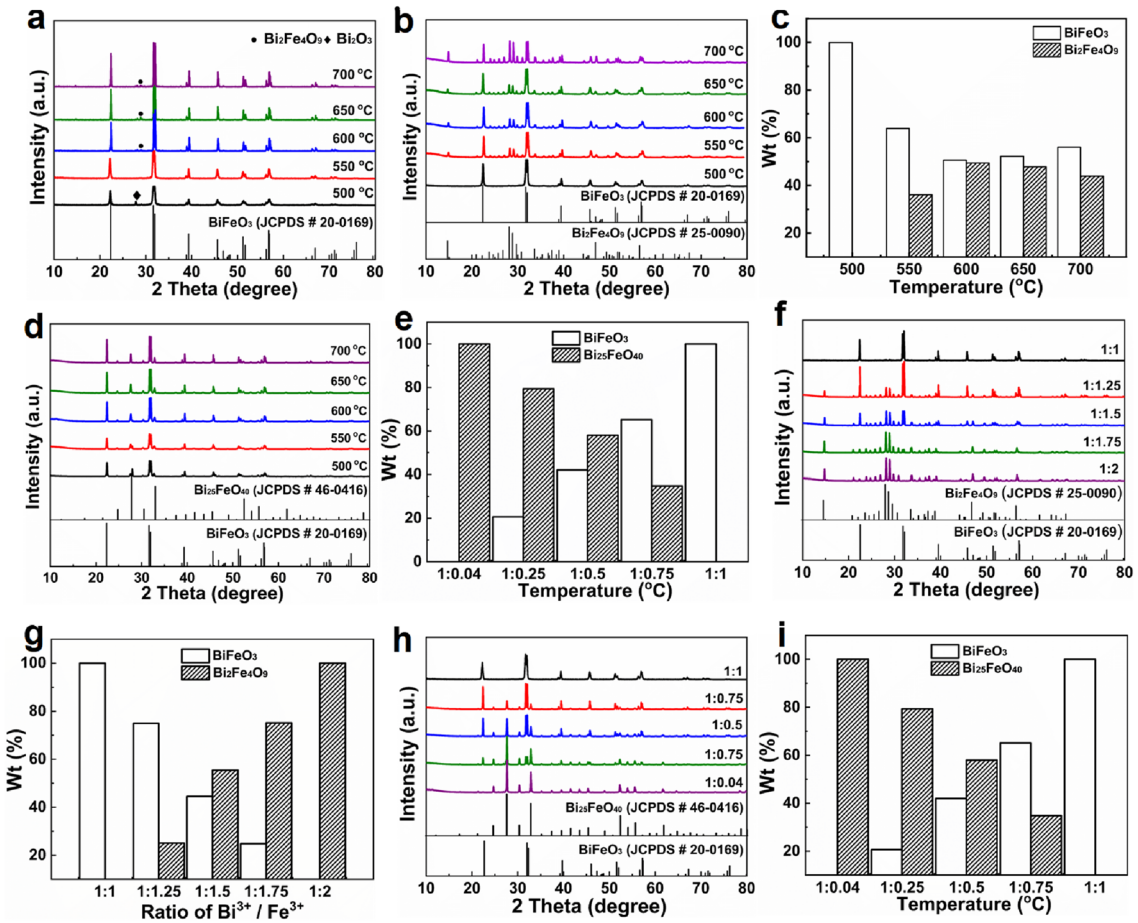

Fig. 1 XRD patterns and phase content of bismuth iron oxide: **a**–**e** Bi3 + /Fe3 + at different calcination temperatures and **f**–**i** Bi3 + /Fe3 + at different stoichiometric ratios

25–0090) phase. This confirms that the temperature can control the generation of bismuth iron oxide. The calculation of the relative content is consistent with that in the literature, where (IA is the intensity of the X-ray diffraction peak on the $BiFeO_3$ (101) plane; IR is the intensity of the X-ray diffraction peak on the $Bi_2Fe_4O_9$ (121), and $Bi_{25}FeO_{40}$ (310) plane is used for all the following calculations of the relative content. As presented in Fig. 1b and c, when Bi^{3+}/Fe^{3+} is 1:1.5, different calcination temperatures indicate that the pure $BiFeO_3$ phase is generated at 500 °C in the presence of excess Fe^{3+} and $Bi_2Fe_4O_9$ phase is generated and its content gradually increases with increasing temperature, indicating that $BiFeO_3$ phase transforms into $BiFeO_3/Bi_2Fe_4O_9$ composite structure at $T > 550$ °C. Thus, the pure $BiFeO_3$ phase can be prepared in the presence of excess Fe^{3+} and at low temperatures [14]. Figure 1d and e shows the influence of different calcination temperatures when Bi^{3+}/Fe^{3+} is 0.75:1, which is the ratio with minimum bandgap width. The temperature renders little effect on the concentration of $BiFeO_3/Bi_{25}FeO_{40}$ composite phase. Figure 1f and g shows the influence of different stoichiometric ratios at 700 °C. The given temperature is selected because it renders the smallest bandgap width. It can be seen that the characteristic diffraction peaks of $BiFeO_3$ and $Bi_2Fe_4O_9$ are quite clear when the molar ratio of Bi^{3+}/Fe^{3+} is 1:1.25 at 700 °C. These peaks clearly indicate the high content of $BiFeO_3$ and low content of $Bi_2Fe_4O_9$. Also, these peaks appear due to the presence of sufficient oxygen. However, both $BiFeO_3$ and $Bi_2Fe_4O_9$ possess similar diffraction peaks when the molar ratio of Bi^{3+}/Fe^{3+} is 1:1.5 and the intensity of the characteristic diffraction peak of $Bi_2Fe_4O_9$ is obviously enhanced when the molar ratio of Bi^{3+}/Fe^{3+} is 1:1.75. Moreover, only the characteristic diffraction peaks of pure $Bi_2Fe_4O_9$ exist and no characteristic diffraction peaks of other secondary phases exist when the molar ratio of Bi^{3+}/Fe^{3+}

is 1:2. In addition, the as-generated pure $BiFeO_3$ and $Bi_2Fe_4O_9$ phases may correspond to the Bi^{3+}/Fe^{3+} stoichiometry ratio of 1:1 [15, 16] and 1:2 [17], respectively, whereas excess Fe^{3+} promotes the transformation of $Bi_2Fe_4O_9$ from $BiFeO_3$ phase, generating intermediate phases according to the molar ratio. As exhibited in Fig. 1h and i, the influence of different stoichiometric ratios is studied at 700 °C, which is a temperature with the smallest bandgap width. Herein, the content composition of $BiFeO_3$ exhibits a slower decay compared to the $Bi_{25}FeO_{40}$ (JCPDS: 46-0416) with the decrease of Bi^{3+}/Fe^{3+} ratio from 1:0.75 to 1:0.04 at 700 °C. Also, different concentrations of $BiFeO_3/Bi_{25}FeO_{40}$ composite phase are formed with the decrease of Fe^{3+} content and only $Bi_{25}FeO_{40}$ exists when the molar ratio of Bi^{3+}/Fe^{3+} is 1:0.04, which corresponds to the Bi^{3+}/Fe^{3+} stoichiometric ratio of 25:1. Furthermore, what effectively avoids the destruction of $BiFeO_3$ crystal structure at high temperatures.

To explore interactions within BFO, XPS analysis determined the valence states and surface chemistry bonds of constituent elements. In high-resolution Bi 4f spectra, the fitted Bi 4f region shows two peaks near 158.68 eV and 164.11 eV, corresponding to Bi $4f_{7/2}$ and Bi $4f_{5/2}$, respectively. This implies the existence of Bi^{3+} valence states in both samples [18]. Moreover, Fe 2p regions split into two peaks for Fe $2p_{3/2}$ and Fe $2p_{1/2}$, which are fitted using the Gaussian–Lorentzian fitting. Spin–orbit binding energies located near 710 eV and 723.5 eV can be attributed to Fe $2p_{3/2}$ and Fe $2p_{1/2}$ of Fe^{2+} species, and the peaks centered near 711 eV and 724.5 eV can be assigned to Fe $2p_{3/2}$ and Fe $2p_{1/2}$ configuration of Fe^{3+} species, respectively. Besides, this demonstrates the chemical valence states of Fe cations in $Bi_{25}FeO_{40}$ and $BiFeO_3/Bi_{25}FeO_{40}$ samples. The peaks located at 713.17 eV and 712.64 eV correspond to Fe^{4+} [19, 20]. The content of Fe species is shown in Table 1. In the high-resolution O 1 s spectra, two peaks with different binding energies are found, which belong to two different oxygen species. The peak near 529 eV can be attributed to the lattice oxygen (O_L), whereas the peak at 530 eV corresponds to the absorbed oxygen species, representing non-lattice oxygen. As shown in Fig. 2a–c, XPS spectra of O 1 s, Bi 4f, and Fe 2p do not exhibit any obvious shift in peak position for $BiFeO_3$ and $BiFeO_3$-$Bi_2Fe_4O_9$, confirming the presence of weaker interactions between $BiFeO_3$ and $Bi_2Fe_4O_9$ and indicating that $BiFeO_3$-$Bi_2Fe_4O_9$ chemical bond interactions are similar to $BiFeO_3$. Furthermore, in the XPS spectra of three materials, the Bi 4f, Fe 2p, and O 1 s peaks of $BiFeO_3/Bi_2Fe_4O_9$ negatively shift around 0.1–0.4 eV as compared to $BiFeO_3$ and $Bi_2Fe_4O_9$, indicating the presence of strong interactions between $BiFeO_3$ and $Bi_2Fe_4O_9$. Moreover, the heterojunction nanostructure properties of $BiFeO_3$–$Bi_2Fe_4O_9$ alloy models and $BiFeO_3/Bi_2Fe_4O_9$ heterojunction nanostructure are evaluated. In Fig. 2d–f, the peaks in high-resolution Bi 4f, Fe 2p, and O 1 s spectra from $BiFeO_3/Bi_{25}FeO_{40}$ heterojunction nanostructure are negatively shifted around 0.1–0.53 eV compared to $BiFeO_3$ and $Bi_{25}FeO_{40}$, indicating the presence of strong electronic interactions between $BiFeO_3$ and $Bi_{25}FeO_{40}$, as exhibited in Fig. 2g–i. Moreover, compared to alloy precipitated ($BiFeO_3$–$Bi_2Fe_4O_9$) by temperature controlled with the heterojunction structure synthesized ($BiFeO_3/Bi_2Fe_4O_9$) by stoichiometric ratio calculation is weaker, the interactions between multiferroic materials ($BiFeO_3/Bi_2Fe_4O_9$) and bismuth-rich materials ($BiFeO_3/Bi_{25}FeO_{40}$) are much stronger than pure bismuth iron oxide phases ($BiFeO_3$, $Bi_2Fe_4O_9$, and $Bi_{25}FeO_{40}$).

The morphologies of as-prepared $Bi_2Fe_4O_9$ and $BiFeO_3/Bi_2Fe_4O_9$ heterojunctions are investigated by SEM, TEM, and HRTEM to confirm the nanosheet-like morphology and heterojunction between $BiFeO_3$ and $Bi_2Fe_4O_9$. As shown in Fig. 3a–c, $Bi_2Fe_4O_9$ displayed obvious agglomeration to form highly polymeric channels and exhibited vivid lattice fringes with an interplanar spacing of 0.316 nm, corresponding to the (121) planes. As shown in Fig. 3d, $BiFeO_3/Bi_2Fe_4O_9$

Table 1 Elemental analyses of Fe using XPS

Sample	Fe $2P_{1/2}$ (eV)			Fe $2P_{3/2}$ (eV)		
$Bi_2Fe_4O_9$	710.1	712.04		723.7	725.64	
$BiFeO_3/Bi_2Fe_4O_9$	710	711.64		723.5	721.38	
$BiFeO_3$	709.69	711.23		723.19	724.73	
$BiFeO_3$–$Bi_2Fe_4O_9$	709.85	711.55		723.43	725.15	
$BiFeO_3/Bi_{25}FeO_{40}$	709.23	710.48	712.64	722.89	723.98	725.68
$Bi_{25}FeO_{40}$	709.33	710.95	713.17	722.73	724.45	727.06

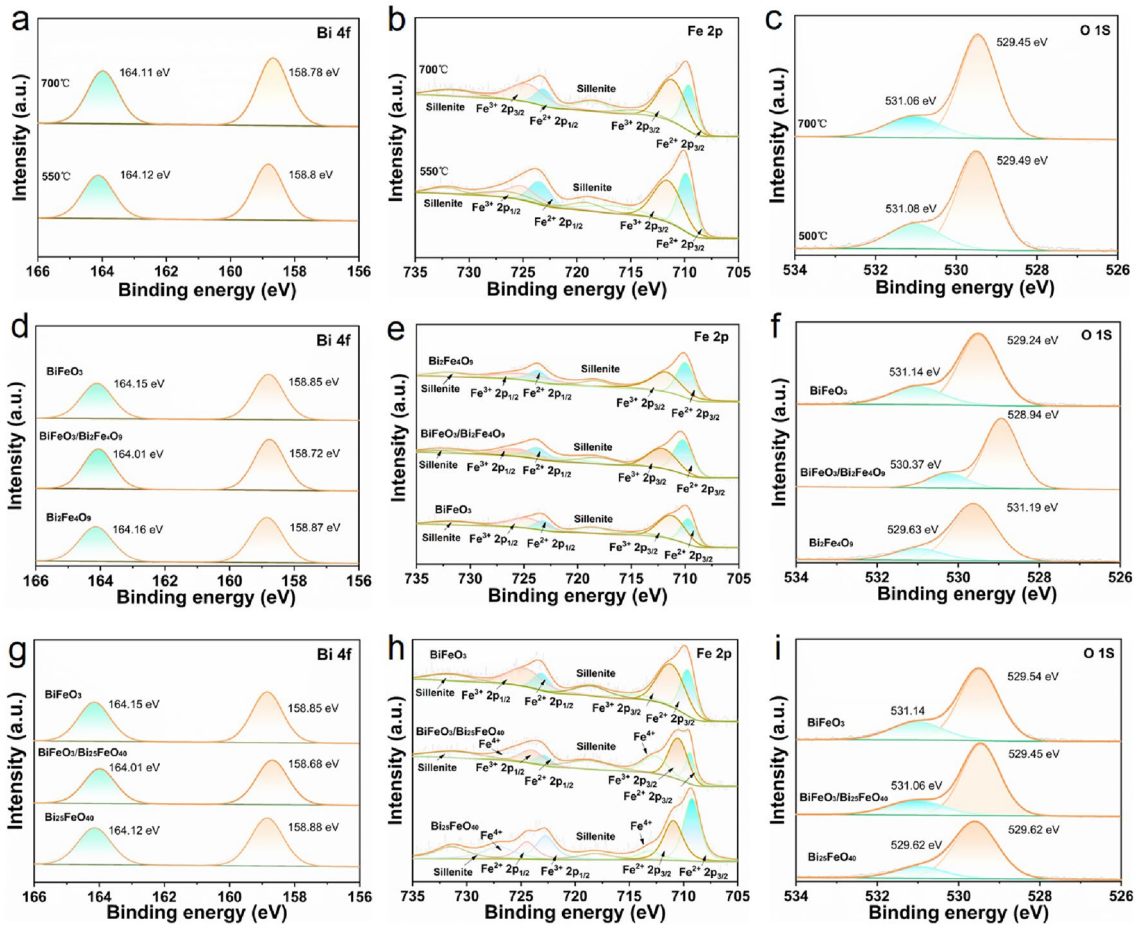

Fig. 2 High-resolution XPS spectra of BFO: **a**–**c** Bi 4f, Fe 2p, and O 1 s of BiFeO3 and BiFeO3-Bi2Fe4O9; **d**–**f** Bi 4f, Fe 2p, and O 1 s of BiFeO3, BiFeO3-Bi2Fe4O9, and Bi2Fe4O9; and **g**–**i** Bi 4f, Fe 2p, and O 1 s of BiFeO3, BiFeO3-Bi25FeO40, and Bi25FeO40

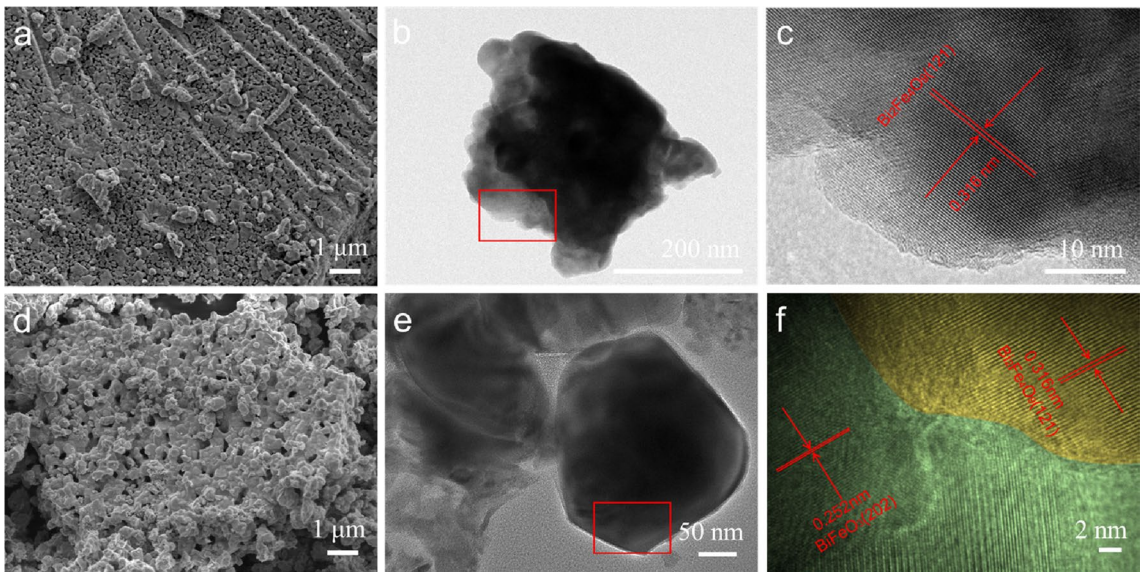

Fig. 3 **a** SEM and **b** TEM images of Bi2Fe4O9 heterojunction nanostructures; **c** HRTEM image of Bi2Fe4O9 nanostructures; **d** SEM and **e** TEM images of BiFeO3/Bi2Fe4O9 heterojunction nanostructure; and **f** HRTEM image of BiFeO3/Bi2Fe4O9 nanostructures

exhibits pores formed due to extensive agglomeration and the surface morphology becomes relatively loose compared to $Bi_2Fe_4O_9$. As displayed in Fig. 3e and f, the observed angle between two crystallographic planes is consistent with the theoretical value and the lattice spacings of 0.252 nm and 0.316 nm correspond to (202) and (121) planes of $BiFeO_3$ (JCPDS # 25-0090) [21] and $Bi_2Fe_4O_9$ (JCPDS # 20-0169) [22, 23], respectively. These results are consistent with XRD and XPS results. Moreover, the successful incorporation of $Bi_2Fe_4O_9$ into $BiFeO_3/Bi_2Fe_4O_9$ confirms that the proposed preparation method realizes the construction of heterojunction nanostructures.

Furthermore, SEM, TEM, and HRTEM images are observed to further analyze the heterojunction and nanosheet morphologies. Figure 4a–c displays loose irregular massive nanosheet-like morphology. Also, the HRTEM image exhibits well-defined lattice fringes with an interplanar spacing of 0.32 nm, corresponding to (310) crystal planes of $Bi_{25}FeO_{40}$. As shown in Fig. 4d, what exhibits relatively loose and irregular block-like morphology and the surface exhibits obviously different grain boundaries compared to $Bi_{25}FeO_{40}$. As exhibited in Fig. 4e and f, $d_{(202)} = 0.252$ may be the lattice spacing of $BiFeO_3$ [21] and another lattice spacing of $d_{(622)} = 0.325$ may correspond to $Bi_{25}FeO_{40}$ (JCPDS # 46-0416). Meanwhile, the material is also identified as $BiFeO_3$ and $Bi_{25}FeO_{40}$ by XRD, as shown in Fig. 1. Elemental maps (Fig. 4g–i) demonstrate the corresponding elemental distribution, which is consistent with the observations, indicating that the grain boundaries of $BiFeO_3$ and $Bi_{25}FeO_{40}$ are formed. Combined with XPS, it can be inferred that strong interactions exist between $BiFeO_3$ and $Bi_{25}FeO_{40}$, confirming that a certain interfacial effect exists between $BiFeO_3$ and $Bi_{25}FeO_{40}$.

As shown in Fig. 5, the UV–vis diffuse reflectance absorption spectra exhibit a red shift from the UV region to the visible region. In the visible band, the spectral lines are shifted toward the red end of the

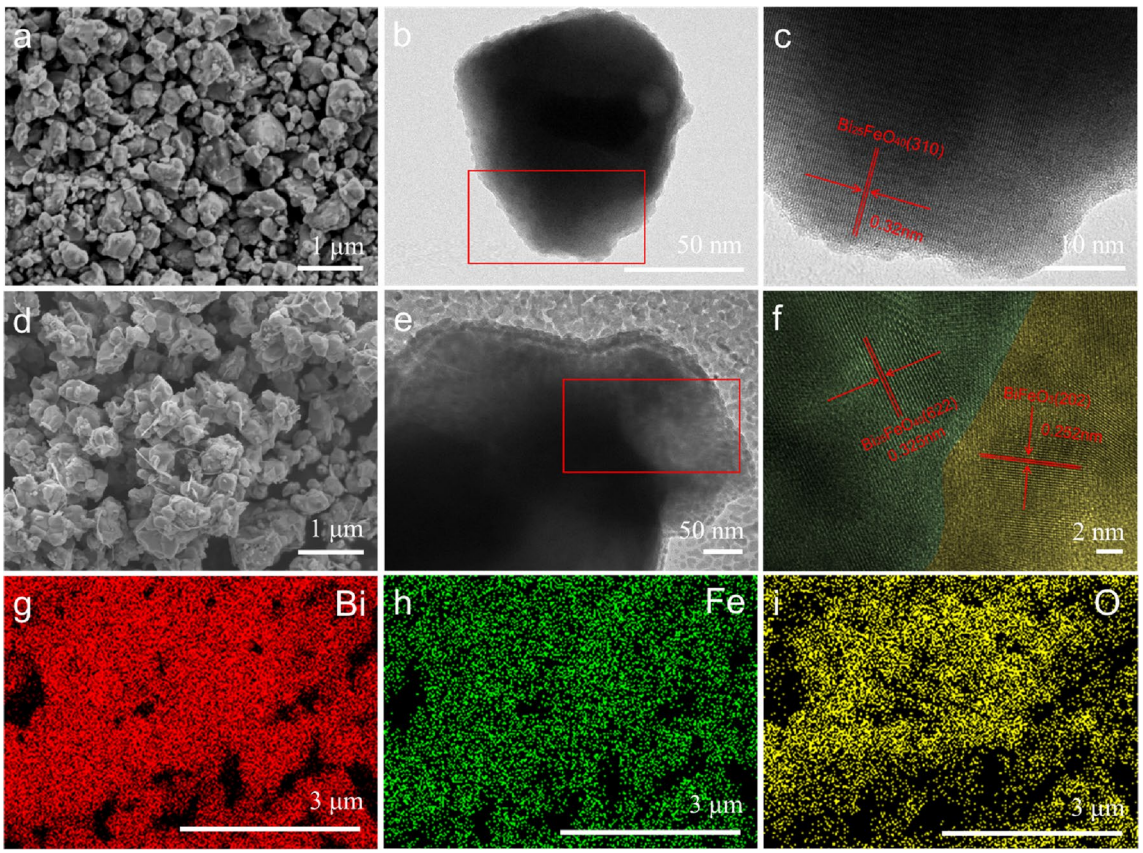

Fig. 4 **a** SEM and **b** TEM images of Bi25FeO40 nanostructures; **c** HRTEM image of Bi25FeO40 nanostructures; **d** SEM and **e** TEM images of BiFeO3/Bi25FeO40 heterojunction nanostructure; **f** HRTEM image of BiFeO3/Bi25FeO40 heterojunction nanostructures; and **g–i** EDS elemental maps of Bi, Fe, and O in BiFeO3/Bi25FeO40 heterojunction nanostructures

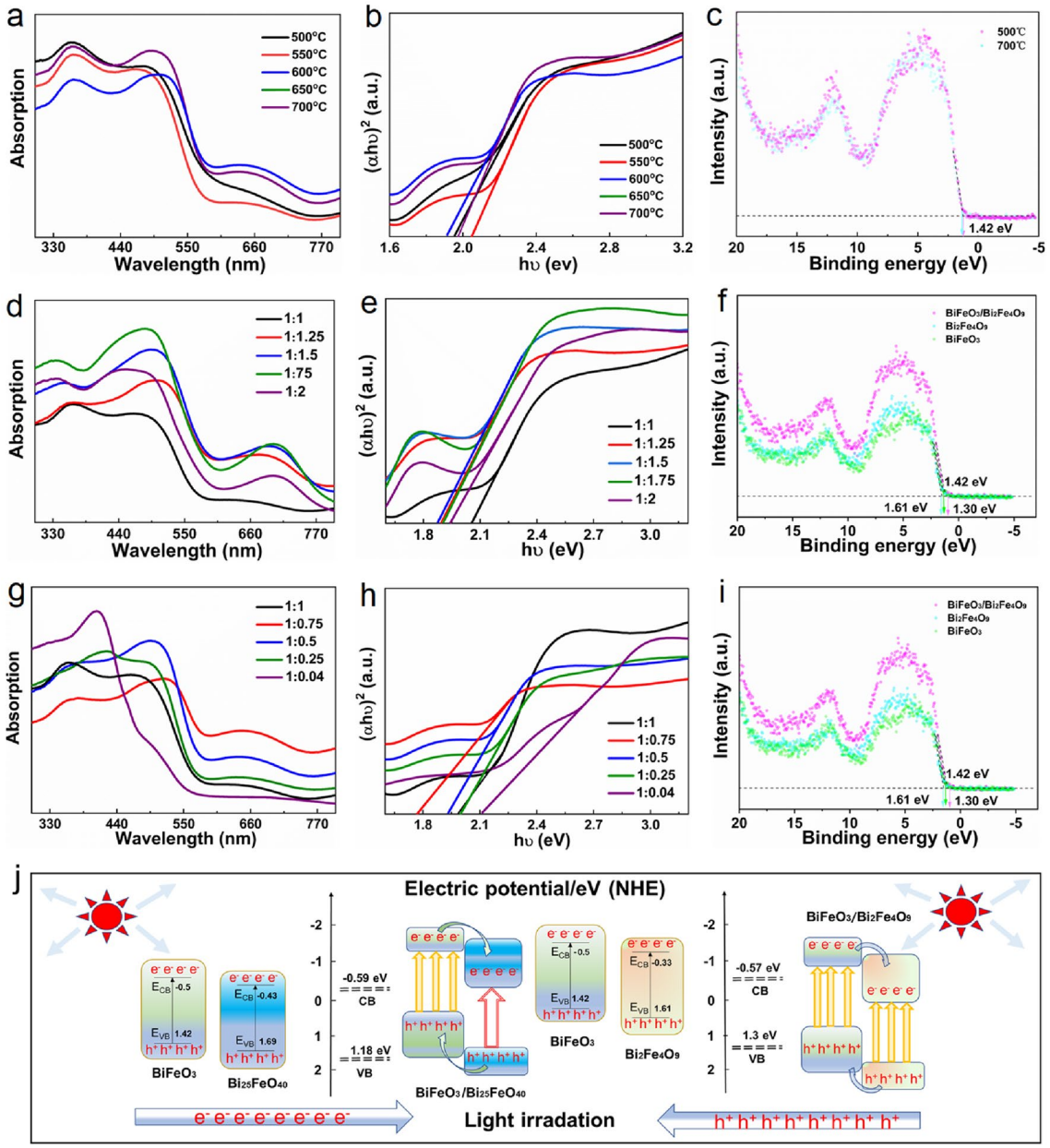

Fig. 5 UV–vis DRS spectra, Kubelka–Munk curves, Mott–Schottky curves, and nanostructured heterostructures of bismuth ferrite oxide materials: **a**–**c** at different calcination temperatures with Bi3 + /Fe3 + stoichiometric ratio of 1:1; **d**–**i** with different molar ratios of Bi3 + /Fe3 + at the calcination temperature of 700 oC; and **j** as-formed BiFeO3/Bi2Fe4O9 and BiFeO3/Bi25FeO40 heterogeneous nanostructures

spectrum by a certain distance. One should note that bismuth ferrite oxide exhibits light absorption properties around 500–600 nm. The corresponding forbidden bandwidths and optical bandgap of the tested sample are fitted with the Tauc equation based on the relationship between $(\alpha hv)^2$ and hv [24]. As shown in Fig. 5a and b, the magnitude of the forbidden bandwidths at 500 °C, 550 °C, 600 °C, 650 °C, and 700 °C is 1.96 eV, 2.05 eV, 1.98 eV, 1.98 eV, and 1.92 eV, respectively. The contents of the forbidden bandwidth are shown in Table 2, illustrating that the energy bandgap of bismuth ferrite oxide nanostructures is changed in the range of 1.92–2.05 eV by controlling the calcination temperature. In addition, the forbidden bandwidth at

Table 2 The bandgap at different calcined temperatures with Bi^{3+}/Fe^{3+} stoichiometric ratio of 1:1

Sample	Temperature (at 700 °C)	Forbidden bandwidths (eV)
1	500	1.96
2	550	2.05
3	600	1.98
4	650	1.98
5	700	1.92

500 °C is significantly smaller than at 550 and 650 °C, which is probably due to the generation of Bi_2O_3/$BiFeO_3$ at 500 °C [25]. As the temperature increases to 700 °C, the forbidden bandwidth decreases and the grains become denser [21]. This proves the conjecture that agglomeration occurs during the high-temperature calcination process. Furthermore, bismuth-rich materials ($BiFeO_3/Bi_{25}FeO_{40}$) are better than multiferroic materials ($BiFeO_3/Bi_2Fe_4O_9$). As shown in Fig. 5d, e, g, and h, the optical bandgap for different molar ratios of Bi^{3+}/Fe^{3+} (1:2, 1:1.75, 1:1.5, 1:1.25, 1:1, 1:0.75, 1:0.5, 1:0.25, and 1:0.04) is found to be 1.94 eV, 1.90 eV, 1.87 eV, 1.89 eV, 1.92 eV, 1.77 eV, 1.93 eV, 1.99 eV, and 2.12 eV, respectively. The contents of the forbidden bandwidth are shown in Table 3, indicating that the bandgap width of heterojunction nanostructure materials ($BiFeO_3/Bi_2Fe_4O_9$ and $BiFeO_3/Bi_{25}FeO_{40}$) is smaller than the pure bismuth iron oxide phase ($BiFeO_3$, $Bi_2Fe_4O_9$, and $Bi_{25}FeO_{40}$), which is consistent with XPS results. Moreover, bismuth-rich materials ($BiFeO_3/Bi_{25}FeO_{40}$) are better than multiferroic materials ($BiFeO_3/Bi_2Fe_4O_9$). As exhibited in Fig. 5c, f, and i, the Mott–Schottky curves (representing the values of E_{VB}) of $BiFeO_3$-$Bi_2Fe_4O_9$ are highly similar to $BiFeO_3$, indicating that the precipitated impurities render a little influence on the structure of bismuth iron oxide, as revealed by XPS results. In addition, E_{CB} can be given as follows:

$$E_{VB} = X - E_e + 0.5E_g, \tag{1}$$

$$E_{CB} = E_{VB} - E_g. \tag{2}$$

E_e refers to the energy of free electrons on the hydrogen scale (~4.5 eV), X represents the geometric mean of electronegativity, and E_g corresponds to the bandgap of the semiconductor compound. E_{VB} of $Bi_2Fe_4O_9$, $BiFeO_3/Bi_2Fe_4O_9$, $BiFeO_3$, $BiFeO_3/Bi_{25}FeO_{40}$, and $Bi_{25}FeO_{40}$ is found to be 1.61 eV, 1.3 eV, 1.42 eV, 1.18 eV, and 1.69 eV, respectively, whereas E_{CB} is found to be − 0.33 eV, − 0.57 eV, − 0.5 eV, − 0.59 eV, and − 0.43 eV, respectively. The contents of the bandgaps are shown in Table 4, indicating that the heterojunction materials are more prone to electron–hole transitions. Figure 5j presents the schematic illustration of the as-formed heterostructure of $BiFeO_3/Bi_2Fe_4O_9$ and $BiFeO_3/Bi_{25}FeO_{40}$.

To further compare the intrinsic activity of bismuth ferrite oxide, the bandgap widths and corresponding crystallite sizes of heterojunction nanostructures at different calcination temperatures were calculated. From the diffuse reflectance spectrum, the Kubelka–Munk function can be used to estimate the optical absorption edge energy (Figure b, e). The forbidden bandwidths change significantly when the wavelength is around 600 nm, and the spectral lines of the spectrum move toward the red end and the wavelength becomes longer, indicating a significant red shift phenomenon (Figure a, d). The forbidden bandwidths of $BiFeO_3/Bi_2Fe_4O_9$ and $BiFeO_3/Bi_{25}FeO_{40}$ at 500 °C, 550 °C,

Table 3 The forbidden bandwidths of samples with different Bi^{3+}/Fe^{3+} stoichiometric ratios at 700 °C

Sample	Ratio of Bi^{3+}/Fe^{3+} (at 700 °C)	Forbidden bandwidths (eV)
1	1:2	1.94
2	1:1.75	1.90
3	1:1.5	1.87
4	1:1.25	1.89
5	1:1	1.92
6	1:0.75	1.77
7	1:0.5	1.93
8	1:0.25	1.99
9	1:0.04	2.12

Table 4 The bandgap of bismuth iron oxide at 700 °C

Sample	E_{VB} (eV)	E_{CB} (eV)
$Bi_2Fe_4O_9$	1.61	− 0.33
$BiFeO_3/Bi_2Fe_4O_9$	1.3	− 0.57
$BiFeO_3$	1.42	− 0.5
$BiFeO_3/Bi_{25}FeO_{40}$	1.18	− 0.59
$Bi_{25}FeO_{40}$	1.69	− 0.43

600 °C, 650 °C, and 700 °C are 1.94/1.91 (eV), 1.99/1.91 (eV), 1.90/1.85 (eV), 1.90/1.84 (eV), and 1.87/1.77 (eV), respectively, as shown in Table 5. The activity of these bismuth ferrite oxide materials is also supported by comparing their bandgap width, while bandgap width of $BiFeO_3$/$Bi_{25}FeO_{40}$ material is smaller than $BiFeO_3$/$Bi_2Fe_4O_9$ material. The crystallite size can be generally calculated using Scherrer's equation, as described elsewhere [26]. After the continuous calcination temperature tests, crystallite size exhibits different variations, where the crystallite size of $BiFeO_3$ and $Bi_{25}FeO_{40}$ materials exhibits a severe increase and $Bi_2Fe_4O_9$ crystals exhibits a little change in crystallite size (Fig. 6c, f and Supplementary Fig. 1). This indicates that the temperature promotes the growth of $BiFeO_3$ and $Bi_{25}FeO_{40}$ grains, and the higher the temperature, the larger the grain size of $BiFeO_3$ and $Bi_{25}FeO_{40}$ grains. In addition, the different Bi^{3+}/Fe^{3+} ratio also affects the granularity of $BiFeO_3$, $Bi_2Fe_4O_9$, and $Bi_{25}FeO_{40}$ materials as demonstrated in (Supplementary Fig. 2, 3).

4 Conclusion

In conclusion, the desired phase composition, heterojunction nanostructure, and crystallite size of bismuth iron oxide, with an optimal concentration of Fe^{3+}, were successfully prepared by the sol–gel method. The experimental results reveal that $BiFeO_3$/$Bi_2Fe_4O_9$ and $BiFeO_3$/$Bi_{25}FeO_{40}$ heterojunction nanostructures display strong interactions between $BiFeO_3$-$Bi_2Fe_4O_9$ and $Bi_{25}FeO_{40}$. Besides, this bandgap width of $BiFeO_3$/$Bi_2Fe_4O_9$ and $BiFeO_3$/$Bi_{25}FeO_{40}$ heterojunction nanostructures is smaller than that of

Table 5 Forbidden bandwidths at different calcination temperatures with Bi^{3+}/Fe^{3+} stoichiometric ratios of 1:1.5 and 1:0.75

Sample (°C)	Forbidden bandwidths (eV) of $BiFeO_3$ and $Bi_2Fe_4O_9$		Crystallite size of $BiFeO_3$ and $Bi_2Fe_4O_9$		Critical size of $BiFeO_3$ and $Bi_{25}FeO_{40}$	
500	1.94	1.91	101.26	53.0	42.9	30.2
550	1.99	1.91	230.8	56.4	60.9	40.3
600	1.90	1.85	165.1	58.0	64.1	44.7
650	1.90	1.84	195.9	61.3	79.5	61.3
700	1.87	1.77	195.9	65.5	81.25	63.1

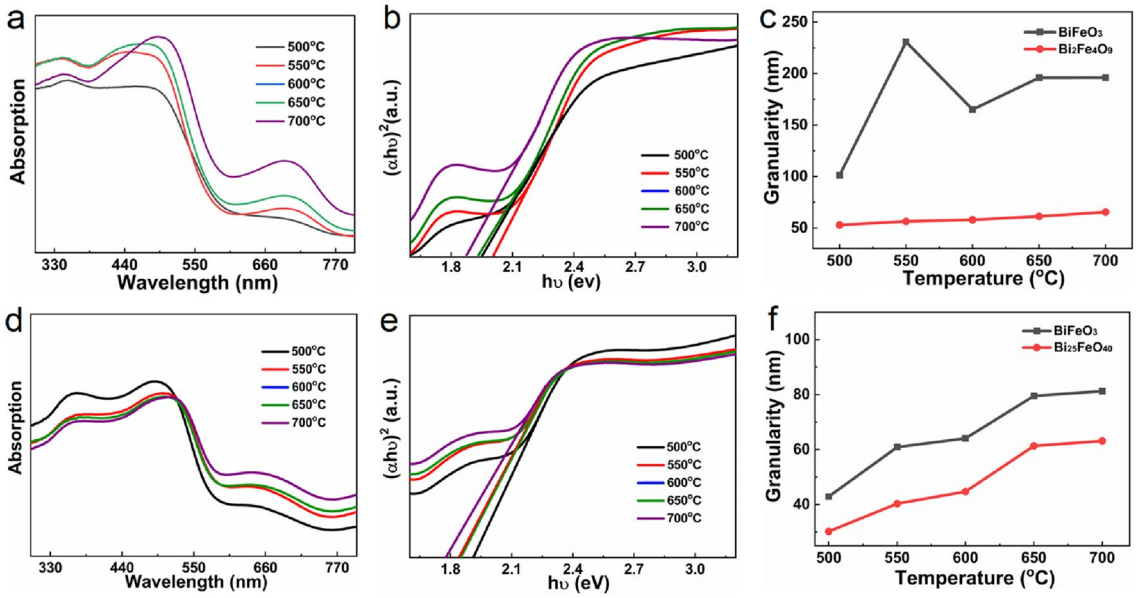

Fig. 6 UV–vis DRS spectra, Kubelka–Munk curves, Mott–Schottky curves, and granularity variation of bismuth ferrite oxide materials at different calcination temperatures of 500 oC, 550 oC, 600 oC, and 650 oC with Bi3 + /Fe3 + ratio of 1:1.5 and 1:0.75

$BiFeO_3$, $Bi_2Fe_4O_9$ and $Bi_{25}FeO_{40}$ materials. At the same time, synthesizing heterojunction, increasing calcination temperature, and reducing Fe^{3+} concentration can precisely control the heterojunction structure, phase composition, grain size, and narrow bandgap of the materials. In addition, $BiFeO_3/Bi_{25}FeO_{40}$ heterojunction has obvious grain boundaries and minimum bandgap. These findings provide pathways for the photocatalytic application of bismuth iron oxide and redox reactions. Meanwhile, the crystallite size plays an important role in controlling the optical, magnetic, electrical, and catalytic properties. Overall, these results have far-reaching implications from the viewpoint of Fe^{3+} content on the structure and performance of bismuth oxide.

Author contributions

CX contributed to investigation, data curation, and writing of the original draft. YW contributed to the conception of the study. QW performed the data analyses and wrote the manuscript. JL performed the data analyses and wrote the manuscript. LY contributed significantly to manuscript preparation. All authors have read and approved the manuscript.

Funding

Jian Li reports financial support was provided by the National Natural Science Foundation of China (22168043). Long Yan reports financial support was provided by Science and Technology Plan Project of Shaanxi Province of China (2016KTZDGY08-04–01). Long Yan reports financial support was provided by Science and Technology Plan Project of Shaanxi Province of China (2020TD-031). Yufei Wang reports financial support was provided by Science and Technology Plan Project of Shaanxi Province of China (2021GY-165). Jian Li reports financial support was provided by Science and Technology Plan Project of Shaanxi Province of China (20JC039). Yufei Wang reports financial support was provided by the Nature Scientific Research Foundation of Shaanxi Provincial Education Office of China (21JP148). Long Yan reports financial support was provided by Joint Funds of Dalian National Laboratory For Clean Energy, CAS and Yulin University (LHJJ10).

Data availability

Some data can be provided if required.

Code availability

Some data can be provided if required.

Declarations

Conflict of interest The authors declare that they have no known competing financial interests or personal relationships that could have appeared to influence the work reported in this paper.

Ethical approval Not Applicable.

Supplementary Information The online version contains supplementary material available at https://doi.org/10.1007/s10854-023-11576-3.

References

1. M. Zhang, M.S. Cao, Q.Q. Wang, X.X. Wang, W.Q. Cao, H.J. Yang, J. Yuan, A multifunctional stealthy material for wireless sensing and active camouflage driven by configurable polarization. J. Mater. Sci. Technol. **132**, 42–49 (2023). https://doi.org/10.1016/j.jmst.2022.05.046

2. R.R. Awasthi, S.K. Trivedi, V.S. Chandel, M. Shariq, H.J. Alathlawi, S.P. Singh, Effect of Zn doping on structural/microstructural, surface topography, and dielectric properties of $Bi_2Fe_4O_9$ polycrystalline nanomaterials. ACS Omega **8**, 15960–15967 (2023). https://doi.org/10.1021/acsomega.2c07604
3. T. Zhang, Y. Shen, Y. Qiu, Y. Liu, R. Xiong, J. Shi, J. Wei, Facial synthesis and photoreaction mechanism of $BiFeO_3$/$Bi_2Fe_4O_9$ Heterojunction nanofibers. ACS Sustain. Chem. Eng. **5**(6), 4630–4636 (2017). https://doi.org/10.1021/acssuschemeng.6b03138
4. L. Wu Yt, G.M. Han, Xu. Sm, Lh. Guo, Controllable synthesis and catalytic activity of bismuth silicate: Thin-layered photocatalysts with the effect of template agent. Ceram. Int. **49**, 6996–7004 (2023). https://doi.org/10.1016/j.ceramint.2022.10.141
5. Y. Liu, H. Guo, Y. Zhang, W. Tang, X. Cheng, W. Li, Heterogeneous activation of peroxymonosulfate by sillenite $Bi_{25}FeO_{40}$: singlet oxygen generation and degradation for aquatic levofloxacin. Chem. Eng. J. **343**, 128–137 (2018). https://doi.org/10.1016/j.cej.2018.02.125
6. A. Kirsch, M.M. Murshed, M. Schowalter, A. Rosenauer, T.M. Gesing, Nanoparticle precursor into polycrystalline $Bi_2Fe_4O_9$: an evolutionary investigation of structural. Morphol. Opt. Vibrat. Prop. J Phys Chem C **120**, 18831–18840 (2016). https://doi.org/10.1021/acs.jpcc.6b04773
7. A. Kirsch, M.M. Murshed, P. Gaczynski, K.D. Becker, T.M. Gesing, $Bi_2Fe_4O_9$: structural changes from nano- to microcrystalline state. Zeitschrift für Naturforschung B **71**, 447–455 (2016). https://doi.org/10.1515/znb-2015-0227
8. E. Zhu, S. Zhao, H. Du, Y. Ma, K. Qi, C. Guo, Z. Su, X. Wang, Z. Wu, Z. Wang, Construction of $Bi_2Fe_4O_9$ red phosphorus heterojunction for rapid and efficient photoreduction of Cr(VI). J. Am. Ceram. Soc. **104**, 5411–5423 (2021). https://doi.org/10.1111/jace.17782
9. D. Wang, X. Dong, Y. Lei, C. Lin, D. Huang, X. Yu, X. Zhang, Fabrication of Mn/P co-doped hollow tubular carbon nitride by a one-step hydrothermal–calcination method for the photocatalytic degradation of organic pollutants. Catal. Sci. Technol. **18**, 5709–5722 (2022). https://doi.org/10.1039/D2CY01107G
10. M. Peng, Y. Yu, Z. Wang, X. Fu, Y. Gu, Y. Wang, K. Zhang, Z. Zhang, M. Huang, Z. Cui, F. Zhong, P. Wu, J. Ye, T. Xu, Q. Li, P. Wang, F. Yue, F. Wu, J. Dai, C. Chen, W. Hu, Room-temperature blackbody-sensitive and fast infrared photodetectors based on 2D Tellurium/Graphene Van der Waals heterojunction. ACS Photonics **9**, 1775–1782 (2022). https://doi.org/10.1021/acsphotonics.2c00246
11. X. Li, L. Wu, S. Cheng, C. Chen, P. Lu, First-principles study on optoelectronic properties of Cs_2PbX_4-$PtSe_2$ van der Waals heterostructures. RSC Adv. **12**, 2292–2299 (2022). https://doi.org/10.1039/D1RA08574C
12. N. Mwankemwa, H.E. Wang, T. Zhu, Q. Fan, F. Zhang, W. Zhang, First principles calculations investigation of optoelectronic properties and photocatalytic CO_2 reduction of $(MoSi_2N_4)_5$-n/$(MoSiGeN_4)$n in-plane heterostructures. Res. Phys. **37**, 105549 (2022). https://doi.org/10.1016/j.rinp.2022.105549
13. M.I. Morozov, N.A. Lomanova, V.V. Gusarov, Specific features of $BiFeO_3$ formation in a mixture of Bismuth(III) and Iron(III) Oxides. Russ. J. Gen. Chem. **73**, 1676–1680 (2003). https://doi.org/10.1023/B:RUGC.0000018640.30953.70
14. J. Wei, Y. Liu, X. Bai, C. Li, Y. Liu, Z. Xu, P. Gemeiner, R. Haumont, I.C. Infante, B. Dkhil, Crystal structure, leakage conduction mechanism evolution and enhanced multiferroic properties in Y-doped $BiFeO_3$ ceramics. Ceram. Int. **42**(12), 13395–13403 (2016). https://doi.org/10.1016/j.ceramint.2016.05.106
15. S.W. Lee, C.S. Kim, Growth of multiferroics $BiFeO_3$ thin films by sol–gel method. J. Magn. Magn. Mater. **304**(2), 772–774 (2006). https://doi.org/10.1016/j.jmmm.2006.02.219
16. J.H. Xu, H. Ke, D.C. Jia, W. Wang, Y. Zhou, Low-temperature synthesis of $BiFeO_3$ nanopowders via a sol–gel method. J. Alloy. Compd. **472**, 473–477 (2009). https://doi.org/10.1016/j.jallcom.2008.04.090
17. P. Psathas, Y. Georgiou, C. Moularas, G.S. Armatas, Y. Deligiannakis, Controlled-phase synthesis of $Bi_2Fe_4O_9$ & $BiFeO_3$ by flame spray pyrolysis and their evaluation as non-noble metal catalysts for efficient reduction of 4-nitrophenol. Powder Technol. **368**, 268–277 (2020). https://doi.org/10.1016/j.powtec.2020.04.059
18. M. Pooladi, H. Shokrollahi, S.A.N.H. Lavasani, H. Yang, Investigation of the structural, magnetic and dielectric properties of Mn-doped $Bi_2Fe_4O_9$ produced by reverse chemical co-precipitation. Mater. Chem. Phys. **229**, 39–48 (2019). https://doi.org/10.1016/j.matchemphys.2019.02.076
19. X. Wang, M. Zhang, P. Tian, W.S. Chin, C.M. Zhang, A facile approach to pure-phase $Bi_2Fe_4O_9$ nanoparticles sensitive to visible light. Appl. Surf. Sci. **321**, 144–149 (2014). https://doi.org/10.1016/j.apsusc.2014.09.166
20. Y. Wu, S. Wang, Y. Gao, X. Yu, H. Jiang, B. Wei, Z. Lü, In situ growth of copper-iron bimetallic nanoparticles in A-site deficient Sr2Fe1.5Mo0.5O6-δ as an active anode material for solid oxide fuel cells. J. Alloys Compd. **926**,

166852 (2022). https://doi.org/10.1016/j.jallcom.2022.166852

21. R. Verma, A. Chauhan, K.M. Neha, R. Batoo, M. Kumar, E.H. Hadhi, Raslan, effect of calcination temperature on structural and morphological properties of bismuth ferrite nanoparticles. Ceram. Int. **47**(3), 3680–3691 (2021). https://doi.org/10.1016/j.ceramint.2020.09.220
22. Y. Xiong, M. Wu, Z. Peng, N. Jiang, Q. Chen, Hydrothermal synthesis and characterization of $Bi_2Fe_4O_9$ nanoparticles. Chem. Lett. **33**(5), 502–503 (2004). https://doi.org/10.1246/cl.2004.502
23. J.T. Han, Y.H. Huang, R.J. Jia, G.C. Shan, R.Q. Guo, W. Huang, Synthesis and magnetic property of submicron $Bi_2Fe_4O_9$. J. Cryst. Growth **294**(2), 469–473 (2006). https://doi.org/10.1016/j.jcrysgro.2006.07.006
24. J. Luo, L. Wang, Z. Sun, P. Liu, Y. Lai, L. Zhu, H. Guo, Novel bismuth ferrite nanopowder prepared by polyethylene glycol-assisted two-step solid-state reaction: synthesis and magneto-optical properties. Ceram. Int. **47**(3), 3514–3519 (2021). https://doi.org/10.1016/j.ceramint.2020.09.194
25. X. Yan, R. Pu, R. Xie, B. Zhang, Y. Shi, W. Liu, G. Ma, N. Yang, Design and fabrication of Bi_2O_3/$BiFeO_3$ heterojunction film with improved photoelectrochemical performance. Appl. Surf. Sci. **552**, 149442 (2021). https://doi.org/10.1016/j.apsusc.2021.149442
26. M. Fu, Z. Hongjian, Optical, magnetic, ferroelectric properties and photocatalytic activity of $Bi_2Fe_4O_9$ nanoparticles through a hydrothermal assisted sol-gel method. Russ. J. Phys. Chem. A **93**, 2079–2086 (2019). https://doi.org/10.1134/S0036024419100169